



Cite this: *Nanoscale*, 2025, **17**, 4455

Plasmonic heating by indium tin oxide nanoparticles: spectrally enabling decoupled near-infrared theranostics†

Nicol Caetano-Zeballos,^{a,b} Leyre Aldaz-Caballero,^{a,c} Jesús Giráldez-Martínez,^d Lucas V. Besteiro,^{d,e} Marta Quintanilla,^{d,f} Riccardo Marin^{d,*a,c,g} and Antonio Benayas^{d,*a,b,c}

All-optical theranostic systems are sought after in nanomedicine, since they combine in a single platform therapeutic and diagnostic capabilities. Commonly in these systems the therapeutic and diagnostic/imaging functions are accomplished with plasmonic photothermal agents and luminescent nanoparticles (NPs), respectively. For maximized performance and minimized side effects, these two modalities should be independently activated, *i.e.*, in a decoupled way, using distinct near infrared (NIR) wavelengths: a radiation window wherein photon-tissue interaction is reduced. Yet, to date, a fully decoupled NIR theranostics system is not available. Finding plasmonic NPs working in that range and without spectral overlap with the absorption and emission of state-of-the-art NIR luminescent NPs requires the development of new materials specifically designed for this purpose. To address this limitation, we herein present water-dispersible indium tin oxide (ITO) NPs whose surface plasmon resonance was tuned for exclusive operation in the third biological window (NIR-III, 1500–1800 nm). That leaves available the first and second biological windows, in which diagnostic tools are typically working. Both the microwave-assisted synthesis and the water-transfer protocol were optimized to obtain NPs with maximum light-to-heat conversion capabilities, owing to their small size and reduced aggregation in aqueous media. Proof-of-concept experiments showed that the lack of overlap between the absorption of ITO NPs and the absorption/emission of model near infrared luminescent species (the widely used Nd^{3+} -doped NPs) is an asset when devising an all-optical theranostics platform. The obtained results set the stage for the development of a new generation of high-performance, all-optical theranostic systems with minimized side effects.

Received 11th October 2024,
Accepted 8th January 2025

DOI: 10.1039/d4nr04212c

rsc.li/nanoscale

Introduction

Within the biomedical context, light-to-heat conversion is a physical process used for imaging, diagnosis, and therapy purposes, having reached in some cases the stage of clinical

translation.^{1,2} For instance, photoacoustic imaging (PAI) relies on the periodic heat generated upon pulsed optical excitation to create acoustic waves *via* the thermoelastic effect.^{1,2} On the other hand, photothermal therapy (PTT) can either directly eradicate malignancies (*e.g.* tumors) or be an adjuvant factor in the context of other therapies, following a controlled local temperature increase.³ Irrespective of the specific application, light-to-heat conversion is frequently performed by nanoparticles (NPs) able to absorb the excitation photons from light sources and convert locally their optical energy into heat.⁴ Plasmonic NPs, which can efficiently release heat upon optical excitation resonant with their surface plasmon,⁵ are arguably prime candidates for application requiring light-to-heat conversion. This is because of their high molar extinction coefficient alongside their spectral tunability, granted by compositional and geometry tuning.⁵

One advanced application of plasmonic NPs is their combination with luminescent NPs to obtain a theranostics nanoplatform.^{6–8} Therein, the plasmonic moiety translates the absorbed optical energy into heat acting as photothermal

^aNanomaterials for BioImaging Group (nanoBIG), Departamento de Física de Materiales, Universidad Autónoma de Madrid (UAM), Madrid 28049, Spain.
E-mail: antonio.benayas@uam.es, riccardo.marin@uam.es

^bNanomaterials for Bioimaging Group (nanoBIG), Instituto Ramón y Cajal de Investigación Sanitaria (IRYCIS), Hospital Ramón y Cajal, Madrid 28034, Spain

^cNicolás Cabrera University Institute of Materials Science, Universidad Autónoma de Madrid (UAM), Madrid 28049, Spain

^dCINBIO, Universidad de Vigo, 36310 Vigo, Spain

^eDepartamento de Física Aplicada, Universidad de Vigo, 36310 Vigo, Spain

^fDepartamento de Física de Materiales, Universidad Autónoma de Madrid (UAM), Madrid 28049, Spain

^gInstitute for Advanced Research in Chemical Sciences (IAdChem) Universidad Autónoma de Madrid, Madrid 28049, Spain

† Electronic supplementary information (ESI) available. See DOI: <https://doi.org/10.1039/d4nr04212c>

agent (*therapeutic* modality),⁹ while the luminescent counterpart can act as the imaging and/or thermal sensing reporter (detection or *diagnostic* modality).¹⁰ Recent studies^{11–13} highlighted how a theranostic platform is more effective and results in reduced side effects when its functionalities are decoupled. In an all-optical system, this means that the diagnostic and therapeutic capabilities can be summoned on demand and orthogonally, using excitation photons of different energy (Fig. 1).

Luminescent NPs regarded as state-of-the-art in biomedical applications are typically excited in the first (NIR-I, 750–950 nm¹⁴) and emit in the second (NIR-II, 1000–1350 nm^{15,16}) biological windows, respectively. In the frame of decoupled theranostics, this leaves the third biological window (NIR-III, 1500–1800 nm^{16,17}) available for photothermal therapy. Nonetheless, currently available plasmonic NPs whose plasmon resonance extends to NIR-III display non-negligible photon extinctions also in NIR-I and NIR-II (e.g., gold nanoshells^{18,19} and CuS NPs^{20,21}), feature extreme geometries making difficult the interaction with living cells (e.g., high aspect-ratio gold nanorods²²), or contains toxic elements (e.g., CdO-based NPs^{23,24}).

In this work we showcase how plasmonic Sn⁴⁺-doped In₂O₃ (ITO) NPs represent the ideal candidate in all-optical decoupled theranostics, owing to a localized surface plasmon resonance almost exclusively located within NIR-III (>1500 nm), along with high heat conversion efficiency (HCE). Specifically, we optimized a microwave-assisted synthesis approach, tailored their surface chemistry to make them water dispersible, and showcased their complementarity with Nd³⁺-doped luminescent NPs for decoupled theranostics.

Results and discussion

Synthesis optimization

The synthesis we implemented was taken from a procedure reported by Kanehara *et al.* and adapted for being carried out

in a microwave reactor. Our approach also differs from the one originally reported in such ref. 25 in that benzoic acid (BA) was tested as organic ligand alongside octanoic acid (OcA).²⁵ For the optimization of the synthesis protocol, we explored the effect of different amounts of Sn⁴⁺ (5, 10, 15 and 20%) and the type of organic acid used as ligand (BA vs. OcA) on the structure, morphology, and properties of the ITO NPs.

First, we observed that changes in the amount of Sn⁴⁺ introduced in the reaction environment between 5 and 20% led only to a minor shift in the energy of the localized surface plasmon resonance (Fig. S6†). This minimal dependence of the optical properties on the Sn⁴⁺ amount seems at odds with previous reports on this material.^{25,26} In principle, one could ascribe this effect to partial Sn⁴⁺ incorporation in the crystalline lattice, with a doping concentration roughly constant despite the Sn⁴⁺ feeding ratio (*i.e.*, nominal amount) as suggested by an invariant peak position in the X-ray diffraction (XRD) patterns of ITO NPs doped with different Sn⁴⁺ amounts (Fig. S4†). However, the fact that there is no peak shift in the XRD patterns does not constitute *per se* a proof of such partial dopant incorporation. Indeed, prior studies have shown that interstitial oxygen, incorporated in the coordination sphere of Sn⁴⁺ for charge compensation, can act against the repulsive forces between atoms and affects the local charge distribution.²⁷ The concentration of interstitial oxygen increases with Sn⁴⁺ concentration, and so does the mentioned effect. That trend reaches such an extent that, above 7%, the lattice constant does not change sizably, and thus XRD peaks are not expected to shift with increasing Sn⁴⁺ incorporation.^{27–29} Thus, to quantitatively test the hypothesis of partial dopant incorporation in the material, total reflection X-ray fluorescence (TXRF) measurements were conducted on the two series of samples, showing an incorporation efficiency between 70 and 80% (Fig. S5†), in accordance with previous reports.²⁵ Hence, Sn⁴⁺ incorporation is partial, yet it scales with the nominal amount of Sn⁴⁺ introduced in the reaction environment. Given the above – and considering how incorporation of additional Sn⁴⁺ amounts beyond 7% has a limited impact on the material's conductivity²⁷ and optical properties²⁵ – we conclude that parameters other than the amount of doped Sn⁴⁺ control the optical properties of our ITO NPs (*i.e.*, aggregation state and depletion layer).

More pronounced effects were observed in the morphology, size, and optical properties upon changing the organic acid used as ligand (BA vs. OcA), while keeping a 10% Sn⁴⁺ doping (Fig. 2). Transmission electron microscopy (TEM) images show the formation of small (7 ± 1 nm), irregular NPs when BA is employed, while larger (19 ± 3 nm), flower-like structures are obtained with OcA (Fig. 2a and b). This difference in size and morphology can be understood in light of the stability of the acid–metal complexes formed *in situ* during the synthesis. Thermogravimetric analysis performed on the two In³⁺ complexes (whose nature was assessed *via* Fourier transform infrared spectroscopy, Fig. S1†) indicates a higher decomposition temperature of indium benzoate compared to the octanoate (Fig. 2c). The higher stability of In³⁺-benzoate suggests that BA

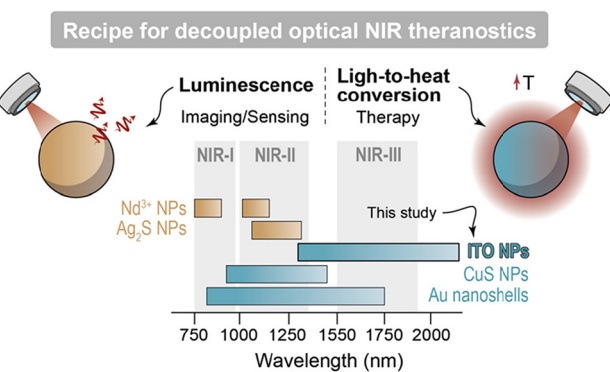


Fig. 1 Scheme of the aim of this study: filling the void in terms of plasmonic nanoparticles capable of absorbing NIR-III radiation while minimally interfering from an optical standpoint with the NIR-I and NIR-II luminescent nanoparticles. Brown color bars display spectral emission ranges, while blue ones display spectral absorption ranges.



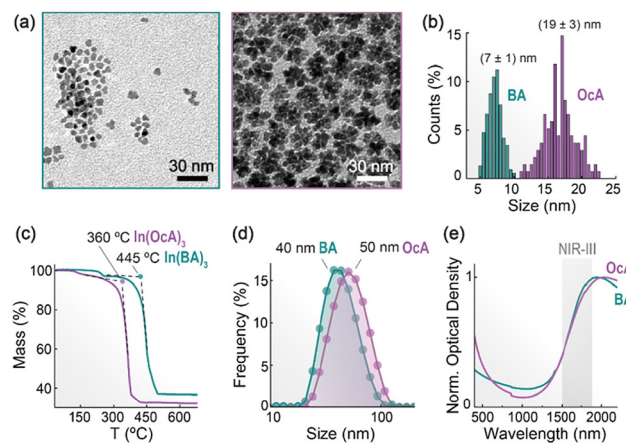


Fig. 2 Effect of the type of organic acid. (a) Representative TEM images of ITO NPs dispersed in hexane synthesized using BA (left) or OcA (right). (b) Size distribution of ITO NPs obtained from the analysis of 200 NPs. (c) Thermograms of the two indium precursors ($\text{In}(\text{BA})_3$ and $\text{In}(\text{OcA})_3$). (d) Hydrodynamic size of the ITO NPs dispersed in hexane. PDI (polydispersity index) values of 0.12 (BA) and 0.11 (OcA) were found, respectively. (e) Normalized UV-Vis extinction spectra – quantitatively measuring optical density – of ITO NPs in tetrachloroethylene.

can bind more strongly than OcA to the ITO NPs surface and hence yield a slower, more controlled growth of the NPs. The lower stability of the octanoate results instead in a faster, less controlled material growth, possibly with a greater overlap between the nucleation and growth regimes.³⁰ In addition, the lower steric hindrance offered by BA compared to OcA is expected to ensure a denser surface coverage during the growth process. As a result, the surface is less accessible to monomers diffusing in solution, limiting the NP growth. These effects combined are considered responsible for the difference in size and morphology observed in ITO-BA and ITO-OcA NPs.

The strong interaction between the aromatic rings³¹ of BA is likely also responsible for the partial aggregation of ITO NPs as evinced from the hydrodynamic size (40 nm) extracted from dynamic light scattering (DLS) measurements, which is sizably larger than the size measured from TEM images (7 nm) (Fig. 2d). The position of the localized surface plasmon resonance (LSPR) peak shows a slight dependence on these features, with the larger nanoflowers showing a more red-shifted maximum compared to the individual, smaller NPs (Fig. 2e). This observation agrees with the results presented by Yang *et al.*²⁶ and follows from the complex nature of the plasmonic resonance in ITO NPs. Milliron and co-workers^{32,33} have extensively shown that the nanoparticle size and extension of the surface depletion layer synergistically contribute to determining the magnitude of the active core responsible for the plasmonic effect in ITO NPs. An interpretation of these features, supported by theoretical modelling, is provided further below.

Upon studying the ITO NPs prepared with the two acids, we selected the ones obtained using BA to carry out further tests. This is because their reduced size represents an advantage in

terms of (i) increased photon absorption *vs.* scattering – hence making for more efficient light-to-heat converters – (ii) reduced scattering at lower wavelengths, which is favourable for the targeted decoupled theranostics, and (iii) suitability for the preparation of hybrid structures, such as core-satellite ones often encountered with plasmonic NPs. Moreover, these ITO NPs synthesised with BA feature their absorption maximum within the region of interest (NIR-III) – see ESI (Fig. S6†).

After the synthesis, the ITO NPs were dispersed in organic solvents like hexane, toluene, or tetrachloroethylene and stored with a slight excess of OA to improve their colloidal stability. Indeed, sometimes, after the washing steps the dispersion appears turbid owing to partial NP aggregation. This is evidenced by an uptick of the extinction spectrum at short wavelengths (Fig. 2e) – arising from increased photon scattering – and more directly from a hydrodynamic size sizably larger than the one observed in TEM micrographs (Fig. 2d).

Transfer to water

Having in mind the use of ITO NPs in biological environments (*i.e.*, aqueous media), we therefore moved to modify their surface to make them water-dispersible while retaining colloidal stability. The method employed for the transfer to water was adapted from a previous report,³⁴ whereby NOBF_4 is employed to strip the hydrophobic ligands from the NP's surface, followed by adsorption of a hydrophilic molecule – in our case, citrate anions (Fig. 3a). An advantage of this method

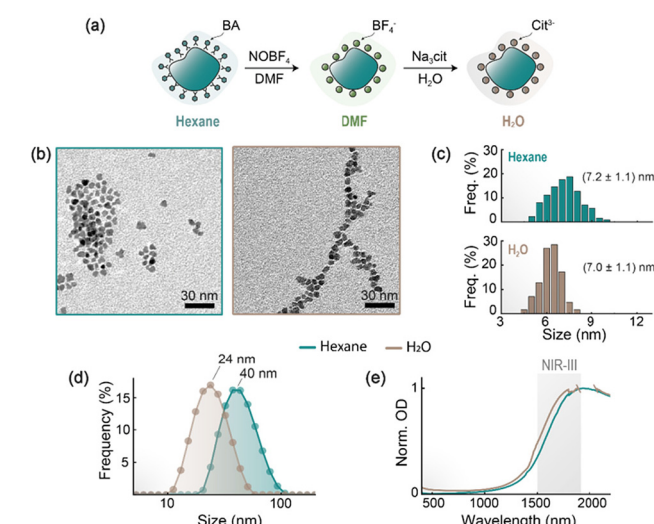


Fig. 3 Transfer to water of ITO NPs synthesized in the presence of BA. (a) Scheme of the steps followed to transfer the synthesized hydrophobic ITO NPs to water. (b) TEM images of ITO NPs in hexane (left) and water (right). (c) Size distribution of ITO NPs in hexane (top) and water (bottom) obtained from the analysis of 300 NPs. (d) Hydrodynamic size of the ITO NPs in hexane and water with PDI (polydispersity index) of 0.12 in both cases. (e) Normalized extinction spectra – quantitatively measuring optical density – of ITO NPs before (in hexane, blue line) and after (in water, brown line) water transfer. Optical density values between 1830 and 2100 nm have been not included in the blue line plot as the water absorption in this range introduces strong perturbation.



resides in the fact that larger aggregates (or soft agglomerates)³⁵ are broken down during the stage of ligand stripping, and water-dispersed ITO NPs decorated with hydrophilic molecules are obtained. TEM images taken before and after the water transfer process corroborate that no relevant modification of the ITO NPs has been produced in shape or size (Fig. 3b and c). On the other hand, DLS measurements reveal that the hydrodynamic size of the citrate-coated ITO NPs dispersed in water (24 nm) is appreciably smaller than the one observed in hexane prior to water transfer (40 nm; Fig. 2d), thus indicating a reduction of the aggregation state. Importantly, the optical properties of the ITO NPs are minimally impacted by the water transfer process, with a slight blue shift (≈ 40 nm) in the extinction spectra compared to as-synthesized ITO NPs dispersed in hexane (Fig. 3e). In fact, electrodynamic simulations (*vide infra*) revealed that the refractive index value of the solvent around ITO NPs does not sizably influence their extinction's spectral shape (Fig. S12†). The retention of the optical properties passing to aqueous environments is a key aspect for the envisaged use of these ITO NPs in the context of NIR decoupled theranostics as highlighted further below.

Computational modelling of ITO NPs optical response

To better understand the response of our ITO NPs as plasmonic resonators, we modelled them using computational methods. We performed full-wave electromagnetic simulations to obtain their optical response in aqueous colloidal dispersion, contrasting two different geometries that mimic the two families of NPs shown in Fig. 2a, obtained using either BA or OcA. We performed our computations modelling ITO with permittivity values from experimental literature.³⁶ Its response is well described by the Drude model (see ESI† for details). The computational results, shown in Fig. 4 alongside a representative optical spectrum of ITO NPs dispersed in water, illustrate several features of these plasmonic NPs. First, the plasmonic band of a small (diameter = 7 nm) ITO nanosphere aligns well with the high-energy edge of the experimental

absorbance, which indicates that the sample is indeed behaving as one would expect from single plasmonic resonators with the optoelectronic properties of ITO. Second, upon contrasting the spectra of the single sphere with the larger, aggregated cluster (see Fig. S10† for their compared geometries), we observe that the latter still retains its main resonance at the single-particle mode, widened by the irregular geometry, and complemented with a secondary peak at longer wavelengths arising from a full-cluster resonance. Cross-sectional maps of these modes can be seen in Fig. S10†. In practice, the cluster presents a broadened spectrum, in comparison with the 7 nm sphere, suggesting that NP aggregation, alongside shape polydispersity and increased damping through surface effects, are behind the broad experimental extinction spectrum. Lastly, our simulations also show that these ITO NPs should be effective light-to-heat converters, in the sense that their plasmonic mode does not decay radiatively (see Fig. S11†), as one would expect from their small sizes and relatively large damping constant of ITO.

Proof-of-concept experiment

We then performed a series of experiments to support our vision of the suitability of the developed ITO NPs in the biomedical context, for decoupled theranostics specifically (Fig. 5). One experiment coarsely reproduces a theranostics system by mixing in the same colloidal aqueous dispersion ITO NPs with Nd³⁺-doped core/shell NaGdF₄ NPs (henceforth, Nd-NPs). The latter moiety constitutes the luminescent component of the theranostics nanoplatform, chosen here because Nd-NPs are often employed for NIR imaging and thermal sensing.^{6,37,38} To better ascertain and benchmark the performance of the ITO NPs, a similar mixed nanofluid was prepared substituting ITO NPs for a staple nanomaterial with plasmonic properties in the NIR-II: copper sulfide (CuS) NPs. The choice of these NPs for comparison purposes – instead of noble metal ones, for example – stems from the fact that both ITO and CuS are semiconductor materials, and their size can be maintained below 10 nm yet achieving NIR-centered plasmonic resonances.²⁰

The two clear spectral advantages of ITO NPs over CuS NPs to decouple optically triggered theranostic systems can be understood from inspection of their extinction spectra when plotted together with the NIR emission of Nd-NPs within NIR-II (Fig. 5a). First, the developed ITO NPs have negligible absorption at the typical excitation wavelength of Nd-NPs (≈ 800 nm). This is not the case for CuS NPs, which are efficiently excited at that wavelength. Therefore, the optical excitation of the luminescent moiety (Nd-NPs) in the theranostics nanofluid would also lead to the simultaneous excitation of the heaters if CuS NPs are used, but that would not be the case if ITO is the plasmonic material of choice. Note that the plasmonic bands are broad, and thus the same would happen regardless of where within NIR-II CuS NPs reach the maximum of their extinction. When 800 nm is used as excitation wavelength, it is anticipated that the ITO NPs will generate negligible heat even in comparison with pure water, while the CuS

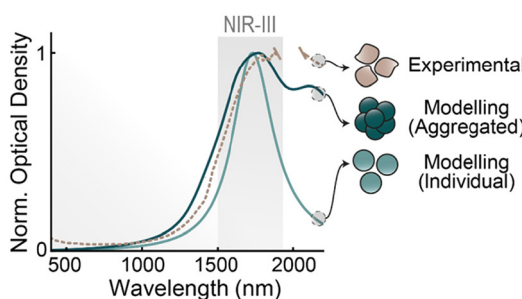


Fig. 4 Simulated optical response. Comparison between experimentally obtained extinction spectra from ITO NPs in water (brown line) and two modelled extinction spectra in full wave numerical simulations: the modelled extinction spectra of a 7 nm ITO nanosphere (single one, blue line) and an 18 nm agglomeration of spherical ITO NPs (aggregated, dark green) are shown.



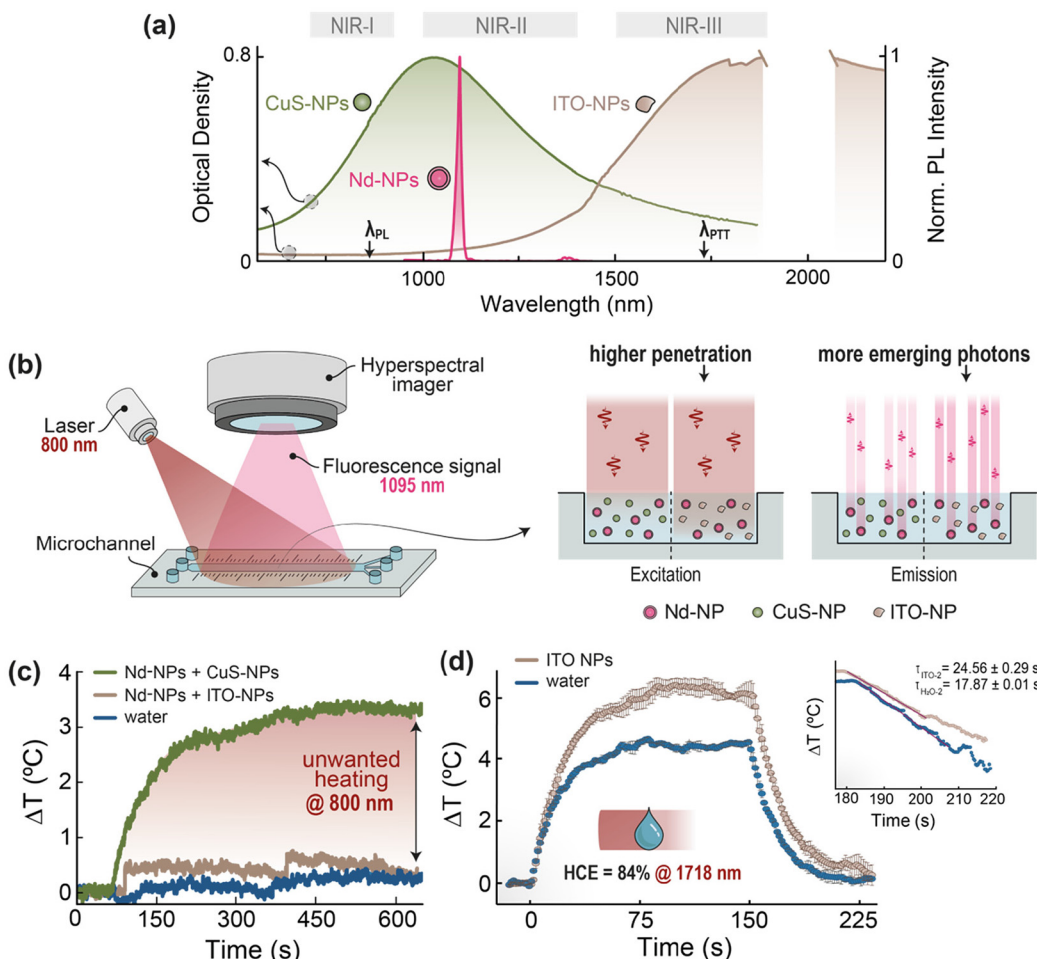


Fig. 5 Comparative validation of the ITO NPs as moiety for decoupled theranostics. (a) Extinction spectra of ITO NPs (brown) and CuS (green) NPs – quantified by optical density – and normalized emission spectrum of core–shell $\text{NaGdF}_4:\text{Nd}^{3+}@\text{NaGdF}_4$ NPs (pink); all the spectra recorded from colloidal dispersions in water. Data around 2000 nm have been deleted, due to strong water absorption in this range. λ_{PL} and λ_{PTT} signal the specific excitation wavelengths used in the experiments (b and c) and (d) respectively. (b) Scheme of a proof-of-concept experiment using two different nanofluids, and detail of the microchannel containing Nd-NPs + CuS NPs (depicted by the zoom on nanofluid at the left), and Nd-NPs + ITO NPs (zoom on nanofluid at the right), for both *Excitation* and *Emission*. (c) Scheme of the procedure followed for the comparison of the heating curves of the two nanofluids equally illuminated at 800 nm, and the water reference. (d) Heating–cooling curves recorded under 1718-nm excitation of distilled water (grey line) and ITO NPs dispersed in water (brown line). The inset shows the fitting of the cooling curves to an exponential decay, used to obtain the *cooling time coefficient*, τ .

NPs can be expected to increase the temperature of the dispersion. Second, the ITO NPs have negligible absorption at the emission wavelength of Nd-NPs. This feature drastically reduces the possibility that the photons emitted by Nd-NPs as the luminescent moiety of a foreseeable theranostic system would get absorbed by the plasmonic moiety. This is clearly not the case if CuS NPs are used as plasmonic heaters, since they show strong absorption between 1000 and 1100 nm, thus likely resulting in an overall weaker signal to be used for imaging/sensing purposes. Again, the same would happen with any other luminescent NP with their emission either in NIR-I or NIR-II.

To prove our point, we performed an experiment (schematized in Fig. 5b) whereby two different nanofluids (Nd-NPs + CuS NPs and Nd-NPs + ITO NPs) were alternatively introduced in a microchannel and excited at 800 nm. The luminescence signal at 1060 nm from the Nd-NPs was recorded by a hyper-

spectral imager. The concentration of the Nd-NPs was the same for both nanofluids under study, while the concentrations of CuS or ITO NPs were adjusted so that both nanofluids present the same optical density value (O.D. = 0.8, measured in the cuvette through an optical path of 0.2 cm) at the maximum of their respective plasmon resonance peaks. In such conditions, the emission intensity recorded from the Nd-NPs + ITO NPs nanofluid was three times higher than the one recorded from the nanofluid containing CuS NPs. That difference was quantified through simple calculations based on the Lambert–Beer law, yielding a nominal penetration depth of 3.2 and 1.0 mm in the presence of either ITO or CuS NPs – these calculations were performed following the procedural described in the ESI (Section S10†).

The negligible thermal load generated by ITO NPs under typical excitation wavelength for Nd-NPs (≈ 800 nm) was

empirically corroborated by an additional experiment where aqueous dispersions of CuS or ITO NPs (at the same concentration used for the experiment in Fig. 5b) were placed in a cuvette and excited with an 800 nm laser while monitoring the temperature with a thermal camera (Fig. 5c). As expected, only the nanofluid Nd-NPs + CuS NPs produces a significant temperature increase of 3 °C, while the Nd-NPs + ITO NPs one shows a minimal thermal increment (≤ 0.5 °C) practically indistinguishable from the one observed with pure water.

Heat conversion efficiency of the ITO NPs

Lastly, we quantitatively assessed the worth of ITO NPs as plasmonic heaters measuring their heat conversion efficiency (HCE), following the widely used approach proposed by Roper *et al.*³⁹ In particular, we used the experimental set up described by Paściak *et al.*⁴⁰ where the measurements are carried out on a droplet of ITO NPs dispersion in water – further details and calculations can be found in Experimental section and ESI (Fig. S13 and S14†). This droplet-approach reduces the measurement time and the optical path, while also decreasing uncertainties on the value of effective heat capacity that are introduced by elements other than the dispersion (*e.g.* cuvette, thermocouple). Through the abovementioned procedural, heating – under optical excitation – and cooling curves from both droplet of water and droplet of ITO NPs dispersed in water were recorded (Fig. 5d). Upon fitting of the cooling curve, shown in the inset of Fig. 5d, the obtained value of HCE, measured under 1718-nm laser excitation, was (84 \pm 7)%. Moreover, following a methodology previously reported and considering that HCE value above was measured on an ITO NPs water dispersion with concentration of 0.81 mg mL⁻¹, an external heating efficiency (eHCE)⁴¹ value of 4.6 L g⁻¹ cm⁻¹ was obtained – which can be considered an HCE value *normalized by mass*. That HCE value above reported, although ranks slightly below the highest reported so far (see Table. S4†), it represents one of the very first reports of HCE measured in the NIR-III window, the other one being plasmonic CuO/CuO₂ truncated nanocubes with a HCE value of 75% using an excitation wavelength of 1550 nm.⁴²

All in all, the above results show that the use of ITO NPs as plasmonic/heating moiety for all-optical decoupled theranostics is feasible, because of negligible photon extinction at both the absorption and emission wavelengths of Nd-NPs (*i.e.*, model NIR luminescent moiety), alongside a high HCE value under NIR-III excitation.

Experimental section

Chemicals and materials

Oleic acid (OA, 90%), tin 2-ethylhexanoate, tetrachloroethylene (99%), copper(II) chloride dihydrate, neodymium(III)acetate, gadolinium(III) oxide and sodium sulfide nonahydrate were purchased from Alfa Aesar. Oleylmine (OAm, 80–90%), indium (III) acetate (99%), benzoic acid (BA, 99%), octanoic acid (OcA, 99%), nitrosonium tetrafluoroborate (97%), ammonium fluor-

ide (98%) and acetic acid (99.8%) were purchased from Acros Organics. Ethanol (96%), *n*-hexane (95%), cyclohexane (95%) and acetone (99.5%) were purchased from Labkem. Chloroform, *N,N*-dimethylformamide (99.5%), methanol (>99.9%) and sodium hydroxide were purchased from Fisher Scientific. Finally, *n*-octylether (96%) was purchased from TCI, and 1-octadecene (90%) was purchased from Thermo Scientific. Distilled water was also used all along the experiments. All reagents and solvents were used without further purification.

ITO NPs synthesis

The ITO NPs were prepared in two steps: the first step entailed the use of a heating mantle, and the second a microwave reactor. Different organic acid ligands – benzoic acid (BA) and octanoic acid (OcA) – and concentrations of Sn⁴⁺ (5, 10, 15, and 20%) were explored as detailed in Table. S1 in the ESI.†

In a typical synthesis of ITO NPs doped, with 10% of Sn⁴⁺ and using BA, the following amounts of reagents were mixed in a 50 mL three-neck round-bottom flask: *n*-octylether (5 mL); indium(III)acetate, In(OAc₃) (0.528 mmol, 157.7 mg); tin(II) ethyl hexanoate (0.072 mmol, 19.4 μ L), BA (1.8 mmol, 219.8 mg), and OAm (5 mmol, 1.6 mL). The mixture was placed under vacuum and heated to 120 °C, temperature at which it was kept for 30 min while stirring to form indium benzoate. The obtained yellow solution was subsequently flushed with Ar for 15 min and transferred to a 35 mL-Pyrex reaction vessel. After purging with Ar, the vial was capped and placed in a microwave reactor (CEM Discover 2.0). The heating process entails the following steps: (i) ramp to 150 °C in 5 min, (ii) hold at 150 °C for 1 h, (iii) ramp to 280 °C in 5 min, (iv) hold at 280 °C for 2 h, (v) rapid cooling to 70 °C. A maximum power of 300 W and medium speed stirring setting were employed in the synthesis. The resulting dark green dispersion was transferred to a 15 mL centrifuge tube, followed by the addition of 1 mL of hexane, 3 mL of ethanol to induce precipitation of the ITO NPs, and centrifugation for 10 min at 3485 rcf. The supernatant was then discarded, and the NPs were redispersed in 3 mL hexane and 25 μ L of oleic acid (OA). The dispersion was sonicated for 5 min, followed by addition of 2 mL of ethanol, and then by a repetition of the same centrifuge step. This process was repeated one more time. Finally, the washed NPs were dispersed in 3 mL of hexane along with 50 μ L of OA and sonicated for 20 min to ensure colloidal stability over time. If a turbid dispersion is observed at any step before ethanol addition, a few drops of OA were added to improve the ITO NPs colloidal stability.

Transfer of NPs to aqueous media (water) using the ligand exchange method

The procedure to transfer ITO NPs into water was adapted from a previously reported work.³⁴ In brief, 250 μ L of ITO NP dispersion was precipitated with 400 μ L of ethanol and centrifuged at 3500 rcf for 5 min. The supernatant was discarded, and the NPs were redispersed in 400 μ L of hexane. A 0.2 M solution of NOBF₄ (15 mg mL⁻¹) in DMF was prepared. The



ITO dispersion was added in 1 mL of the NOBF_4 solution while stirring and left to stir for another 10 min at room temperature (two layers are observed: the NOBF_4 solution and the NP ITO dispersion). The solution was transferred to a centrifuge tube and sonicated for 10 min to obtain a turbid mixture. After that, 6 mL of chloroform was added to dissolve the OA and precipitate the BF_4^- ion-coated NPs. The dispersion was centrifuged at 3000 rcf for 10 min. After discarding the supernatant, 1.5 mL of DMF was added and sonicated until complete redispersion. Then, 4 mL of a 1:1 hexane:toluene mixture was added to induce flocculation of the NPs, followed by centrifugation at 3000 rcf for 5 min. After discarding the supernatant, the NPs were redispersed in 0.5 mL of DMF, followed by addition of 1.5 mL of a 0.4 M aqueous sodium citrate solution. The NPs dispersion was shaken in a vortex for 1 min and sonicated for 10 min to mix the reagents properly. The solution was precipitated with 8 mL of acetone and centrifuged at 3000 rcf for 10 min. Finally, the supernatant was discarded, and the ITO NPs were redispersed in 1.5 mL of water.

Synthesis of CuS NPs and Nd³⁺-doped core/shell NaGdF₄ NPs (Nd-NPs)

Detailed description of the synthesis of the other NPs used for the validation experiment (Fig. 5b) can be found within Section S1 of ESI.†

Characterization

Transmission electron microscopy (TEM). TEM images were taken on JEM1400 Flash, JEOL. Samples were made taking 0.3 mg mL⁻¹ of ITO NPs and dropped into a carbon-coated Cu grid.

X-ray powder diffraction (XRPD). The study of ITO NPs' crystal structure was performed on a Rigaku D/max- γ B diffractometer working in the Bragg–Brentano geometry (θ – 2θ) with a step of 0.03° in the 20–65° range. For sample preparation, dispersion drops were added to the slide, and the solvent evaporated to deposit the dry sample.

Dynamic light scattering (DLS). Hydrodynamic size measurements at room temperature were performed on a Zetasizer Ultra (Malvern Panalytical, Ltd).

Thermogravimetry (TGA). The thermogravimetric study was performed to determine the thermal induced mass change of indium(III) benzoate and indium(III) octanoate precursors with the TGA/DSC STARe System (Mettler Toledo). Thermal analysis was performed from 25 to 700 °C using a heating ramp of 10 °C min⁻¹ under a nitrogen and oxygen atmosphere.

UV-vis-NIR extinction. The UV-VIS-NIR extinction spectra were recorded at room temperature on a spectrophotometer (PerkinElmer Lambda1050), specifically using a 3 nm step in the 350–2500 nm range. The spectra are measured as optical density as a function of the wavelength, being the optical density.

$$\text{OD} = \log_{10} \left(\frac{I_0}{I} \right)$$

where I_0 is the intensity of the incident light, and I the intensity of the transmitted light through the material/nanofluid tested.

Optical density is the actual parameter we measured to quantitatively assess the *extinction*, *i.e.*, the physical phenomenon attributable to the combination of absorption and scattering.

Fourier transform infrared spectroscopy (FTIR). FTIR spectra were recorded in transmission mode with the Spectrum Two instrument (PerkinElmer) in the range 400–4000 cm⁻¹ and a resolution of 4 cm⁻¹. Samples were prepared from KBr pellets containing 1% by weight of the material to be analyzed.

Luminescence emission from nanofluids filling out a micro-channel hyperspectral imager. The power density of the excitation laser (808 nm, LIMO30-F200-DL808, LIMO) was 195 mW cm⁻². The emission of Nd³⁺ nanofluid was collected by a NIR camera (HyperCube, Photon *etc.*), using a long-pass filter (FEL 850, Thorlabs) to select the measurement range (950–1400 nm).

Heat conversion efficiency (HCE) measurements by single droplet method. The experimental approach has been performed using the droplet configuration (Fig. S13†).⁴⁰ The system consists of a 1718 nm laser which irradiates a droplet of an aqueous dispersion of ITO NPs hanging from a needle, a power meter to detect the transmitted laser power. To monitor the temperature of the droplet, a thermal camera (FLIR, E54 24°) was used, with a mounted germanium lens (Thorlabs) to magnify the image. The heating–cooling curves were obtained from the analysis of recorded thermal videos. Upon fitting the recorded cooling curve to an exponential, and applying the thermal equilibrium equation, as given by Roper *et al.*³⁹ heat conversion efficiency is calculated in percentage (see Section 9 of ESI†).

Stability of the ITO NPs in a biological medium. The stability test was performed using two different samples. The first sample consisted of a dispersion of ITO NPs (0.45 mg mL⁻¹) and FBS (10:90 volume proportion), and the second one contained a solution of water and FBS with such volume proportion. DLS and optical extinction measurements were successively conducted at different time points. The DLS measurements were performed using a quartz cuvette with an optical path of 1 cm. The extinction spectrum was measured using a quartz cuvette with an optical path of 0.1 cm to reduce the strong perturbation due to the water absorption between 1830 and 2100 nm.

Interaction of the ITO NPs with cells

Chemicals. Phosphate buffered saline (PBS, Cytiva), MTT solution (1 mg mL⁻¹ in PBS), dimethyl sulfoxide (DMSO, Thermo Scientific) and Dulbecco's modified Eagle's medium (DMEM, Cytiva). Complete medium is based on DMEM, adding 1% Penicillin–Streptomycin (10 000 U mL⁻¹, HyClone) and 10% fetal bovine serum (FBS, Gibco).

Viability assay. The viability assay was done using U87 MG cell line (glioblastoma, epithelial) as cancer model. Initially 5000 cells per well were planted in standard transparent 24-wells plate (Thermo Scientific, Biolite), and 0.5 mL complete medium was added to each well. The cells were cultured



during 24 h. Then, they were incubated with different concentrations (0.02, 0.04, 0.09 and 0.2 mg mL⁻¹) of NPs (each concentration, $n = 4$). The nanoparticles were originally dispersed in water, thus small amounts of these solutions were diluted in complete DMEM for the test. A positive control was prepared adding only complete medium ($n = 4$). An additional control with 100 μ L H₂O (the maximum volume used in the test) in the medium ($n = 2$) was also prepared to consider any possible toxicity from water. Finally, a negative control ($n = 2$) was done adding 0.5 mL DMSO directly to the cells.

Incubation was set to 24 h. After the incubation, the cells were washed with PBS to remove remaining ITO particles, and an MTT viability test was performed. Briefly, 0.5 mL of 9:1 solution of DMEM (without FBS) and MTT solution (1 mg mL⁻¹ in PBS) were added to each well. The plate was left in the incubator for 2 h. After this time, the medium was discarded, and the now formed formazan crystals were dissolved in 0.5 mL DMSO. The plate was then covered with aluminium foil and shook gently for 15 min. Absorbance was measured in a plate reader (Synergy HTX, BioTek) to determine viability. To obtain the concentration of internalized nanoparticles, the final DMSO solution was recovered in Eppendorf tubes and analysed with ICP, using indium as calibration ion.

Conclusions

We have developed novel water-dispersible plasmonic ITO nanoparticles (NPs) as foreseeable building blocks in all-optical decoupled NIR theranostics. Upon optimization of a microwave-assisted synthesis approach and water transfer protocol, we obtained ITO NPs portraying an extinction spectrum dominated by absorption confined within NIR-III. Theoretical modelling within a classical frame predicts optical properties well in line with the experimentally observed ones, also shining light on the effect that nanoparticle aggregation has on the optical response of ITO NPs. Specifically, modelling shows that nanoparticle aggregation widens the plasmonic resonance and generates a redshift. The HCE value, measured to be $84 \pm 7\%$ under ~ 1700 nm excitation (maximum of plasmonic peak), is one of the very few reported values for plasmonic materials with NIR-III extinction and makes a strong case for their use as photothermal agents in the biomedical context. Moreover, it is expected that ITO NPs can be optically targeted with much better *in vivo* spatial accuracy than preexisting plasmonic heaters, as their optical excitation within NIR-III should greatly decrease the scattering induced on the incoming excitation beam by the tissues surrounding the region of interest.

With proof-of-concept experiments, our study spectrally validates the use of ITO NPs in an all-optical decoupled therapeutic system, as they can adequately team up with luminescent NPs currently applied in biomedical applications (excited in NIR-I and emitting in NIR-II) without detrimental spectral overlapping. In such a system, different NIR excitation wavelengths can activate different functions (sensing/imaging or

heating) of the theranostics nanoplatform of which ITO NPs would constitute a building block. Besides, the optical signal from the partner (luminescent) moiety will not see diminished its intensity by ITO NPs absorption.

We foresee a forthcoming *in vivo* theranostic platform – built either embedding the luminescent and heating NPs inside the same scaffold (e.g., ITO and Nd-NPs embedded together into a porous-like nanostructure) or directly joining together the two species in a composite construct – that could be optimized for instance in applications that require real-time monitoring of temperature (luminescence thermometry) while performing photothermal therapy (plasmonic heating). Upon further validation of the nanomaterial in terms of long-term stability and biocompatibility, diverse possibilities can be opened in the biomedical context using plasmonic ITO NPs. For instance, they can be coupled with NIR-III emitting NPs in energy transfer-based assays, or for photoacoustic imaging. As such, we envisage that this study will spur a more in-depth exploration of NIR-III plasmonic NPs for bio-related applications.

Author contributions

Nicol Caetano-Zeballos: data curation, formal analysis, investigation, methodology, visualization, writing – original draft. Leyre Aldaz-Caballero: data curation, formal analysis. Jesús Giráldez-Martínez: data curation, formal analysis, investigation, methodology. Lucas V. Besteiro: conceptualization, investigation, writing – original draft. Marta Quintanilla: conceptualization, validation, supervision, writing – review and editing. Riccardo Marin: conceptualization, formal analysis, methodology, investigation, supervision, validation, visualization, writing – original draft, writing – review and editing. Antonio Benayas: conceptualization, funding acquisition, investigation, methodology, project administration, resources, supervision, validation, writing – original draft, writing – review and editing.

All authors have given approval to the final version of the manuscript.

Data availability

A data availability statement has been provided is <https://zenodo.org/records/13902784>.

Conflicts of interest

There are no conflicts to declare.

Acknowledgements

This work has been supported by project ref. 2019-T1/IND-14014 under Talento program and by project S2022/



BMD-7403 RENIM-CM, both from Comunidad de Madrid (Spain). N. C-Z. acknowledges financial support from Comunidad de Madrid through both INVESTIGO program, contract number INV/09-PIN1-00013.4/2022, and TALENTO grant ref. 2023-5A/IND-28937. M. Q. acknowledges funding support from CNS2023-145169 SAHNDOCAN, funded by MCIN/AEI/10.13039/501100011033 and EU NextGenerationEU/PRTR. R. M. is grateful to the Spanish Ministerio de Ciencia e Innovación for support to research through a Ramón y Cajal Fellowship (RYC2021-032913-I). L. V. B. acknowledges support by MCIN/AEI/10.13039/501100011033 and European Union “NextGenerationEU”/PRT through projects PID2020-118282RA-I00, TED2021-130038A-I00, RYC2021-033818-I, and by Xunta de Galicia under project ED431F 2024/021. JGM acknowledges support by MCIN/AEI/10.13039/501100011033 through project FPU21/03137. A. B. acknowledges funding from Comunidad de Madrid through TALENTO grant ref. 2023-5A/IND-28937.

References

- 1 I.-C. Sun, D. S. Dumani and S. Y. Emelianov, *ACS Nano*, 2024, **18**, 3575–3582.
- 2 J. J. M. Riksen, A. V. Nikolaev and G. van Soest, *J. Biomed. Opt.*, 2023, **28**, 121205.
- 3 X. Cui, Q. Ruan, X. Zhuo, X. Xia, J. Hu, R. Fu, Y. Li, J. Wang and H. Xu, *Chem. Rev.*, 2023, **123**, 6891–6952.
- 4 S. Duan, Y. Hu, Y. Zhao, K. Tang, Z. Zhang, Z. Liu, Y. Wang, H. Guo, Y. Miao, H. Du, D. Yang, S. Li and J. Zhang, *RSC Adv.*, 2023, **13**, 14443–14460.
- 5 Z. He, C. Y. Zhang, Y. Lei, G. Song and Y. Yao, *Mater. Today*, 2023, **62**, 168–189.
- 6 M. Runowski, S. Goderski, J. Paczesny, M. Ksiezopolska-Gocalska, A. Ekner-Grzyb, T. Grzyb, J. D. Rybka, M. Giersig and S. Lis, *J. Phys. Chem. C*, 2016, **120**, 23788–23798.
- 7 M. Quintanilla, I. García, I. De Lázaro, R. García-Alvarez, M. Henriksen-Lacey, S. Vranic, K. Kostarelos and L. M. Liz-Marzán, *Theranostics*, 2019, **9**, 7298–7312.
- 8 E. T. Vickers, M. Garai, S. Bonabi Naghadeh, S. Lindley, J. Hibbs, Q.-H. Xu and J. Z. Zhang, *J. Phys. Chem. C*, 2017, **121**, 13304–13313.
- 9 A. R. Indhu, L. Keerthana and G. Dharmalingam, *Beilstein J. Nanotechnol.*, 2023, **14**, 380–419.
- 10 I. Martinić, S. V. Eliseeva and S. Petoud, *J. Lumin.*, 2017, **189**, 19–43.
- 11 Md. A. Barkat, M. A. Rahman, M. A. Ansari and F. J. Ahmad, in *Nanotheranostics for Diagnosis and Therapy*, ed. Md. A. Barkat, F. J. Ahmad, M. A. Rahman and M. A. Ansari, Springer Nature Singapore, Singapore, 2024, pp. 1–13.
- 12 R. Prasad and K. Selvaraj, *Nanotheranostics*, 2024, **8**, 12–32.
- 13 R. M. Pallares, F. M. Mottaghy, V. Schulz, F. Kiessling and T. Lammers, *J. Nucl. Med.*, 2022, **63**, 1802–1808.
- 14 Z. Yu, X. Fu, S. Zheng and H. Zhang, *J. Lumin.*, 2021, **231**, 117753.
- 15 B. Tang, W. Li, Y. Chang, B. Yuan, Y. Wu, M. Zhang, J. Xu, J. Li and X. Zhang, *Angew. Chem., Int. Ed.*, 2019, **58**, 15526–15531.
- 16 T. Chihara, M. Umezawa, K. Miyata, S. Sekiyama, N. Hosokawa, K. Okubo, M. Kamimura and K. Soga, *Sci. Rep.*, 2019, **9**, 12806.
- 17 X. Zhang, F. Yu, Z. Wang, T. Jiang, X. Song and F. Yu, *Sens. Diagn.*, 2023, **2**, 1077–1096.
- 18 M. Chen, X.-T. Chen, L.-Y. Zhang, W. Meng, Y.-J. Chen, Y.-S. Zhang, Z.-C. Chen, H.-M. Wang, C.-M. Luo, X.-D. Shi, W.-H. Zhang, M.-S. Wang and J.-X. Chen, *J. Nanobiotechnol.*, 2023, **21**, 138.
- 19 A. Plan Sangnier, A. Van De Walle, R. Aupaure, M. Fradet, L. Motte, E. Guénin, Y. Lalatonne and C. Wilhelm, *Adv. Biosys.*, 2020, **4**, 1900284.
- 20 R. Marin, A. Skripka, L. V. Besteiro, A. Benayas, Z. Wang, A. O. Govorov, P. Canton and F. Vetrone, *Small*, 2018, **14**, 1803282.
- 21 R. Marin, J. Lifante, L. V. Besteiro, Z. Wang, A. O. Govorov, F. Rivero, F. Alfonso, F. Sanz-Rodríguez and D. Jaque, *Adv. Healthcare Mater.*, 2020, **9**, 1901627.
- 22 S. Wang, W. Xi, F. Cai, X. Zhao, Z. Xu, J. Qian and S. He, *Theranostics*, 2015, **5**, 251–266.
- 23 Z. Liu, Y. Zhong, I. Shafei, S. Jeong, L. Wang, H. T. Nguyen, C.-J. Sun, T. Li, J. Chen, L. Chen, Y. Losovyj, X. Gao, W. Ma and X. Ye, *Nano Lett.*, 2020, **20**, 2821–2828.
- 24 S. A. Shubert-Zuleta, V. Segui Barragan, M. W. Berry, R. Russum and D. J. Milliron, *ACS Nano*, 2024, **18**, 16776–16789.
- 25 M. Kanehara, H. Koike, T. Yoshinaga and T. Teranishi, *J. Am. Chem. Soc.*, 2009, **131**, 17736–17737.
- 26 K. Ma, N. Zhou, M. Yuan, D. Li and D. Yang, *Nanoscale Res. Lett.*, 2014, **9**, 547.
- 27 N. Yamada, I. Yasui, Y. Li and Y. Nomura, *Jpn. J. Appl. Phys.*, 1999, **38**, 2856.
- 28 P. Psuja, D. Hreniak and W. Strek, *J. Phys.:Conf. Ser.*, 2009, **146**, 012012.
- 29 B. Xu, R. Feng, B. Yang and Y. Deng, *Trans. Nonferrous Met. Soc. China*, 2010, **20**, 643–648.
- 30 I. Halimi, E. M. Rodrigues, S. L. Maurizio, H.-Q. T. Sun, M. Grewal, E. M. Boase, N. Liu, R. Marin and E. Hemmer, *J. Mater. Chem. C*, 2019, **7**, 15364–15374.
- 31 A. Heuer-Jungemann, N. Feliu, I. Bakaimi, M. Hamaly, A. Alkilany, I. Chakraborty, A. Masood, M. F. Casula, A. Kostopoulou, E. Oh, K. Susumu, M. H. Stewart, I. L. Medintz, E. Stratakis, W. J. Parak and A. G. Kanaras, *Chem. Rev.*, 2019, **119**, 4819–4880.
- 32 J. Ephraim, D. Lanigan, C. Staller, D. J. Milliron and E. Thimsen, *Chem. Mater.*, 2016, **28**, 5549–5553.
- 33 S. L. Gibbs, C. M. Staller and D. J. Milliron, *Acc. Chem. Res.*, 2019, **52**, 2516–2524.
- 34 A. Dong, X. Ye, J. Chen, Y. Kang, T. Gordon, J. M. Kikkawa and C. B. Murray, *J. Am. Chem. Soc.*, 2011, **133**, 998–1006.
- 35 G. Nichols, S. Byard, M. J. Bloxham, J. Botterill, N. J. Dawson, A. Dennis, V. Diart, N. C. North and J. D. Sherwood, *J. Pharm. Sci.*, 2002, **91**, 2103–2109.



36 Y. Wang, A. Capretti and L. Dal Negro, *Opt. Mater. Express*, 2015, **5**, 2415.

37 G. Chen, T. Y. Ohulchanskyy, S. Liu, W.-C. Law, F. Wu, M. T. Swihart, H. Ågren and P. N. Prasad, *ACS Nano*, 2012, **6**, 2969–2977.

38 L. Sun, S. Shi, H. Geng, Y. Huang, Y. Qiao, J. Song, L. Yang, C. A. Grimes, X. Feng and Q. Cai, *ACS Appl. Nano Mater.*, 2021, **4**, 11231–11238.

39 D. K. Roper, W. Ahn and M. Hoepfner, *J. Phys. Chem. C*, 2007, **111**, 3636–3641.

40 A. Paściak, A. Pilch-Wróbel, Ł. Marciniak, P. J. Schuck and A. Bednarkiewicz, *ACS Appl. Mater. Interfaces*, 2021, **13**, 44556–44567.

41 A. Paściak, R. Marin, L. Abiven, A. Pilch-Wróbel, M. Misiak, W. Xu, K. Prorok, O. Bezkrovnyi, Ł. Marciniak, C. Chanéac, F. Gazeau, R. Bazzi, S. Roux, B. Viana, V.-P. Lehto, D. Jaque and A. Bednarkiewicz, *ACS Appl. Mater. Interfaces*, 2022, **14**, 33555–33566.

42 M. Shanmugam, N. Kuthala, R. Vankayala, C.-S. Chiang, X. Kong and K. C. Hwang, *ACS Nano*, 2021, **15**, 14404–14418.

